Supporting Information

Heat Charging Towards Electric Energy Saving and High-Efficiency Zn-ion Batteries

Xiaoling Sun,[a] Yitong Li,[a] Dewen Zeng,[a] Zhiwei Zeng,[a] Chen Gong,[a] Changyi Wu,[b] Hongyi Chen[a]*

[a]College of Chemistry and Chemical Engineering, Central South University, Changsha, 410083, Hunan, China.

[b]Department of Physics and Chemistry, Hunan First Normal University, Changsha, 410205, Hunan, China.

*Corresponding author. E-mail: hongyichen@csu.edu.cn (H. C.)

The detailed modification of the Nernst equation

The chemical reaction at cathode and anode in NiHCF/Zn battery is

Cathode: $KNi^{II}Fe^{III}(CN)_6 + K^+ + e^- \rightarrow K_2Ni^{II}Fe^{II}(CN)_6$ (S1)

Anode: $Zn^{2+} + 2e^- \rightarrow Zn$ (S2)

The temperature coefficient of cathode (α_+) and anode (α_-) can be given by the Nernst equation,

$$\alpha_+ = \alpha_+^{\ominus} + \frac{J_1 R}{nF}\ln([K^+]) \quad \text{(S3)}$$

$$\alpha_- = \alpha_-^{\ominus} + \frac{J_2 R}{nF}\ln([Zn^{2+}]) \quad \text{(S4)}$$

where J_1 and J_2 are the correction factors of K^+ and Zn^{2+} ion concentrations, respectively, R is the ideal gas constant, n is the number of electrons transferred in the reaction, and F is the Faraday constant (96485 C·mol^{-1}).

After introducing the high entropy reversible reaction, there are two competitive equations (1) and (2) in zinc anode, the proportion is l and $(1-l)$, the corresponding temperature coefficients are denoted as α_1 and α_2 respectively.

$$\alpha_1 = \alpha_1^{\ominus} + \frac{J_1 R}{nF}\ln([Zn^{2+}]) \quad \text{(S5)}$$

$$\alpha_2 = \alpha_2^{\ominus} - \frac{J_2 R}{nF}\ln([Co^{2+}]^x[SO_4^{2-}]^y[OH^-]^z) \quad \text{(S6)}$$

Where J is the correction factor for ion concentration. Where $\alpha_1^{\ominus}$ and $\alpha_2^{\ominus}$ represent the standard temperature coefficient of the equations (1) and (2).

The total temperature coefficient (α_-) of these two reactions can be described as

$$\alpha_- = \alpha_1 \times l + \alpha_2 \times (1-l) \quad \text{(S7)}$$

For the equilibrium state, the ion concentration can be given by

$$C_{Zn^{2+}} C_{Co^{2+}}^{\ x} C_{SO_4^{2-}}^{\ y} C_{OH^-}^{\ z} = K_{eq} \quad \text{(S8)}$$

where K_{eq} is the equilibrium constant. When the Zn anode loses Δx mol of electrons, m mol of Zn^{2+} form Zn/Co-LDH, where $m=\Delta x(1-l)$, equation (S8) is changed to

$$(C_{Zn^{2+}} + \Delta x - m)(C_{Co^{2+}} - mx)^x (C_{SO_4^{2-}} - my)^y (C_{OH^-} - mz)^z = K_{eq} \quad \text{(S9)}$$

Dividing equation (S8) by (S9) and taking first-order approximation through the Taylor expansion,

$$m\left(\frac{1}{C_{Zn^{2+}}} + \frac{x^2}{C_{Co^{2+}}} + \frac{y^2}{C_{SO_4^{2-}}} + \frac{z^2}{C_{OH^-}}\right) = \frac{\Delta x}{C_{Zn^{2+}}} \quad \text{(S10)}$$

According to equation (S7) and (S10)

$$\alpha_{-} = \alpha_1^{\ominus} + \frac{\alpha_2^{\ominus} - \alpha_1^{\ominus} - U + (M + NHC_{Zn^{2+}})lnC_{Zn^{2+}}}{1 + HC_{Zn^{2+}}} \quad \text{(S11)}$$

where, $H = \frac{x^2}{C_{Co^{2+}}} + \frac{y^2}{C_{SO_4^{2-}}} + \frac{z^2}{C_{OH^-}}$, $N = \frac{J_1 R}{nF}$, $M = \frac{J_2 R}{nF}$ and $U = \frac{J_2 R \ln K_{eq}}{nF}$. Considering that $NHC_{Zn^{2+}}lnC_{Zn^{2+}}$ is very small, α_{-} is approximated to

$$\alpha_{-} \approx \alpha_1^{\ominus} + \frac{\alpha_2^{\ominus} - \alpha_1^{\ominus} - U + MlnC_{Zn^{2+}}}{1 + HC_{Zn^{2+}}} \quad \text{(S12)}$$

The trade-off between energy efficiency and energy density

Indeed, the heat charging strategy enhances energy efficiency, but it concurrently diminishes energy density. The trade-off between energy efficiency and energy density are as follows.

In our research, a heat charging cycle saves 11.23% of electrical energy. If the capacity of the battery is *x* KWh, and the electricity price is 0.65 $/kWh) according to Southern California Edison,[1] the saving cost Y_1 for 1000 cycles is calculated as:

$$Y_1 = 11.23\%\ x \times 1000 \times 0.65\ \$/kWh \quad \text{(S13)}$$

Actually, a charging and discharging range is chosen as 15% to 85% state of charge (SOC), resulting in a 30% loss of energy density compared to normal charging and discharging. Therefore, an additional 30% battery cost is required to maintain the battery performance. If the capacity of the battery is *x* KWh, and the battery price is 210 $/kWh, the additional cost Y_2 is represented as:

$$Y_2 = 30\%\ x \times 210\ \$/kWh \quad \text{(S14)}$$

According to equations (S13) and (S14), Y_1 is 1.16 times that of Y_2, indicating the heat charging strategy has economic advantages. Furthermore, as long as the ratio of electricity price to battery price is greater than 0.27%, our work can demonstrate its economic benefits. The energy shortage and the maturity of battery technology will further highlight the significance of heat charging.

Supplementary Figures

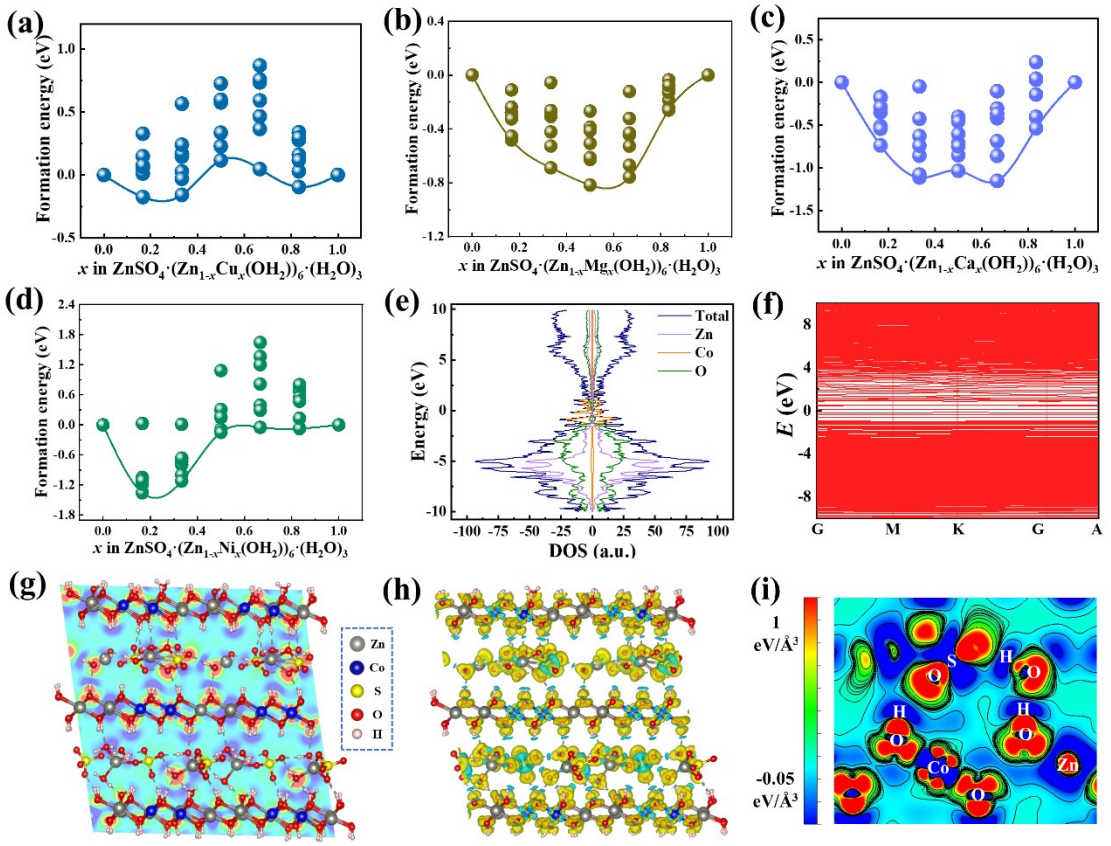

Fig. S1. Formation energy for various element-doped in Zn/M-LDH materials. (a-d) Formation energy (E) as a function of doping concentrations x in Cu-doped (a), Mg-doped (b), Ca-doped (c), and Ni-doped (d), which was calculated by $E=E_{Zn/M\text{-}LDH}-(1-x)E_{Zn\text{-}LDH}-xE_{M\text{-}LDH}$. (e-i) The density of states (e), the energy band diagram (f), the deformation charge density diagram (g), the 3D diagram of differential charge density (h), and the 2D projection of differential charge density (i) of the Zn/Co-LDH materials.

The formation energy (E_{form}) was calculated according to $E_{form} = E_{Mx} - xE_{M1} - (1-x)E_{M0}$, where E_{Mx}, E_{M1} and E_{M0} were the energies of $ZnSO_4{\cdot}(Zn_{1-x}M_x(OH)_2)_6{\cdot}(H_2O)_3$, $ZnSO_4{\cdot}(M(OH)_2)_6{\cdot}(H_2O)_3$ and $ZnSO_4{\cdot}(Zn(OH)_2)_6{\cdot}(H_2O)_3$, respectively. The low formation energy mainly depends on the strength of the *M*-OH bond. The cation of Co(II) undergoes s-p-d hybridization due to the empty d-orbitals, thereby enhancing the strength of *M*-OH bonds.

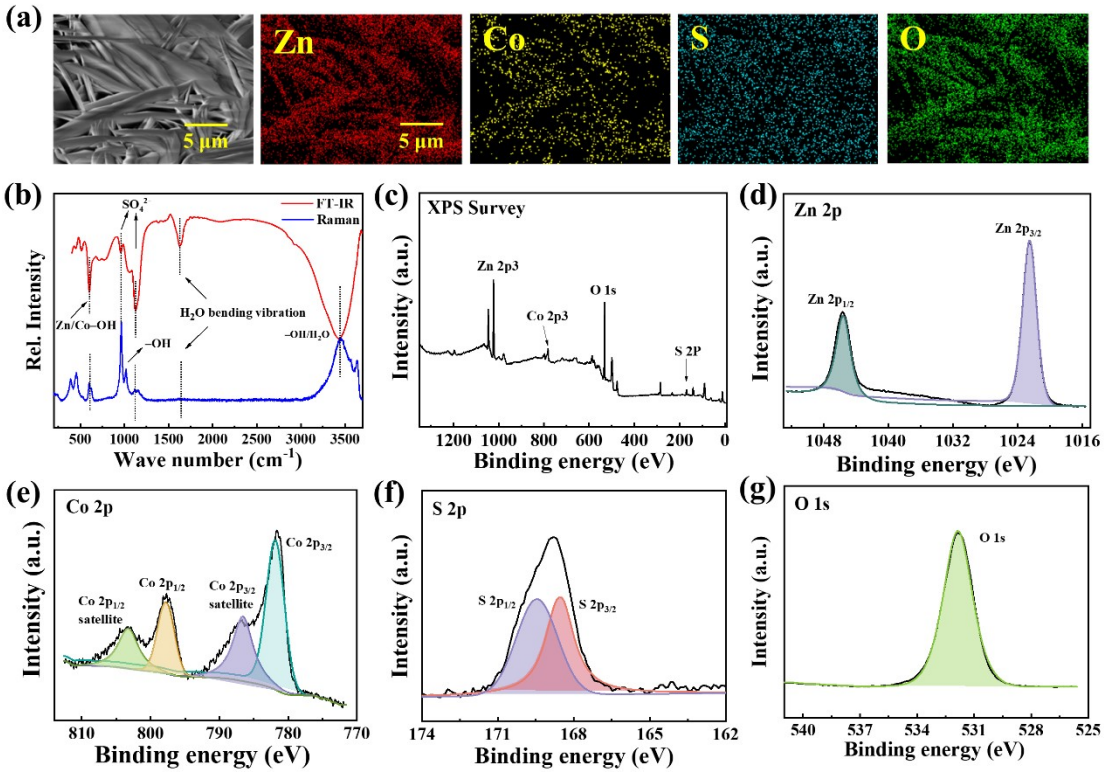

Fig. S2. The characteristic of Zn-LDH powder. (a) The SEM and EDS mapping. (b) The FTIR/Raman spectra. (c-g) The XPS survey (c) and fine scan (d-g). The peak-fitting and analysis of the Co 2p spectrum indicate that the +2 oxidation state of Co exists in Zn/Co-LDH. Moreover, the existence of Co^{2+} in Zn/Co-LDH ensures electron conservation in LDH, consistent with equation (2).

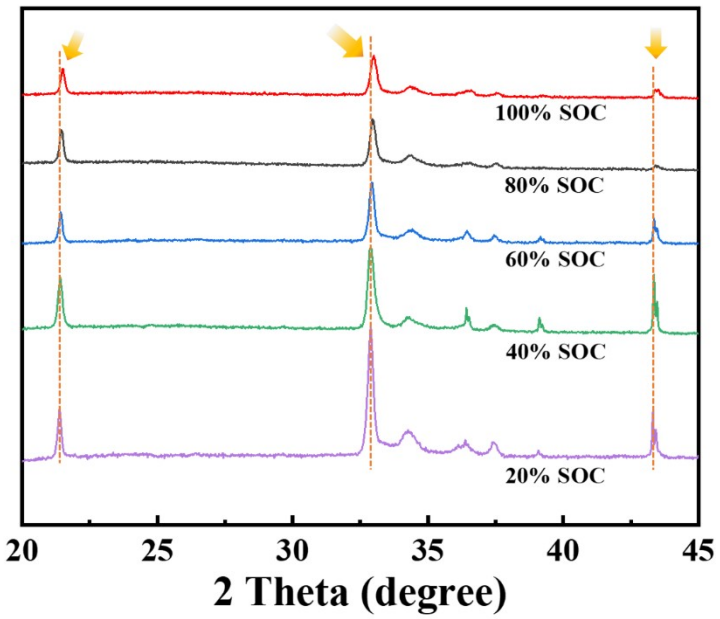

Fig. S3. XRD patterns of Zn/Co-LDH at different battery's capacities. From 20%SOC to 100%SOC, the diffraction peaks slightly shift to a higher angle region, indicating that slight Co^{2+} replaces the Zn^{2+}.[2-4]

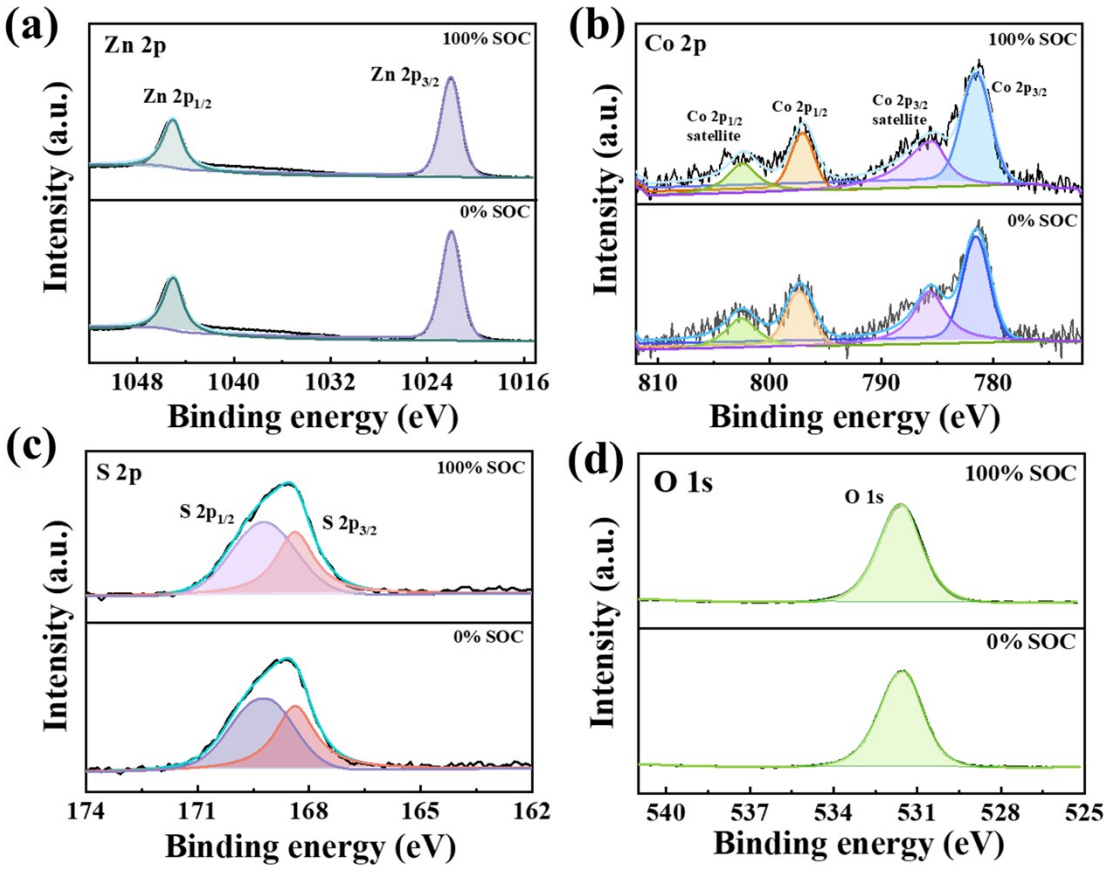

Fig. S4. XPS spectrums for Zn/Co-LDH at fully discharged (0%SOC) and fully charged states (100% SOC) in the (a) Zn 2p, (b) Co 2p, (c) S 2p, and (d) O 1s regions. The results show that the valence states of the Zn, Co, S, and O elements in Zn/Co-LDH remain unchanged at 0% and 100% SOC. It further illustrates that the +2 oxidation state of Co exists in Zn/Co-LDH.

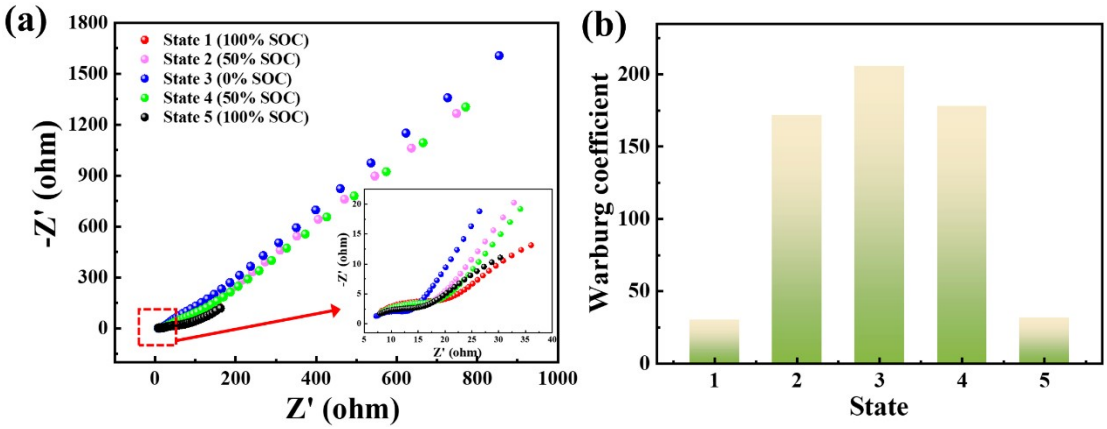

Fig. S5. During the charging and discharging process (a) Nyquist plots of NiHCF/Zn-LDH battery (inset shows the magnified region between 5 Ohm and 36 Ohm), (b) The Warburg coefficient in five states. The EIS measurements were carried out in five states, denoted as state 1 - fully charged (100% SOC), state 2 - half discharged (50% SOC), state 3 - fully discharged (0% SOC), state 4 - half charged (50% SOC), and state 5 - fully charged (100% SOC), respectively. It shows that the Warburg coefficient ($^{\sigma_w}$) gradually increases during the discharging process while decreasing during the charging process, indicating that the formation of LDH materials during the discharging process hinders ionic diffusion, leading to smaller ion mobilities.

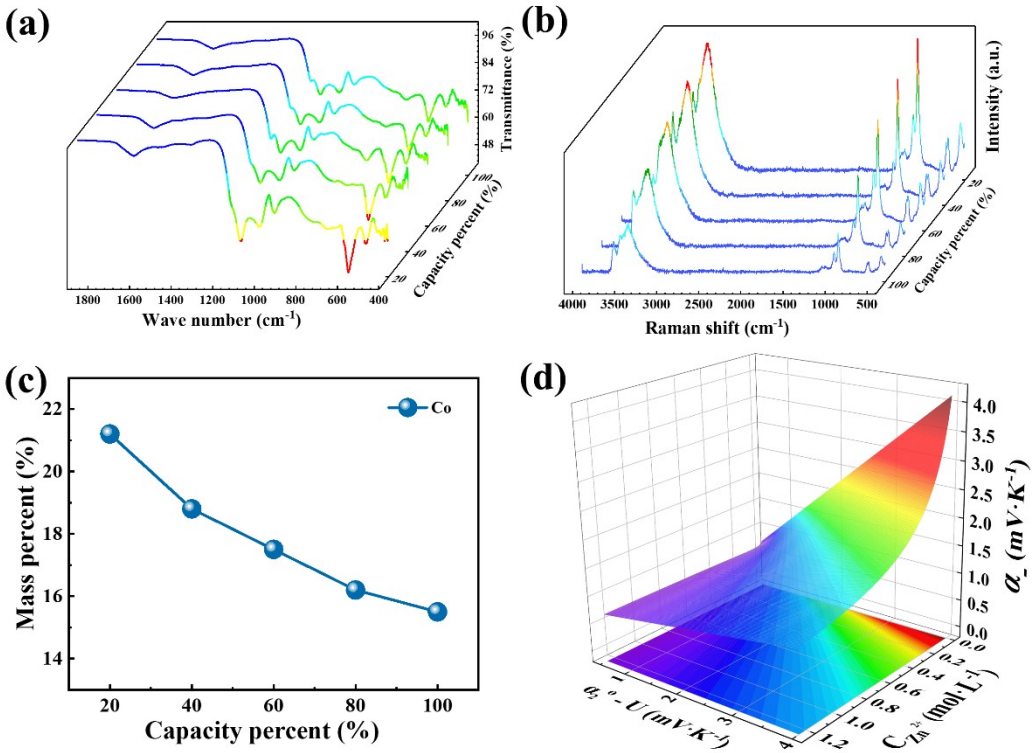

Fig. S6. Characterization of the Zn-LDH material electrode at different battery's capacities. (a) Variation of characteristic peaks by FTIR spectra. (b) Variation of characteristic peaks by Raman spectra. (c) Mass percent of Co content. (d) Temperature coefficient α_{-} as a function of C_{Zn}^{2+} and $\alpha_2^{\ominus}$-U (see the details in equations S5-12).

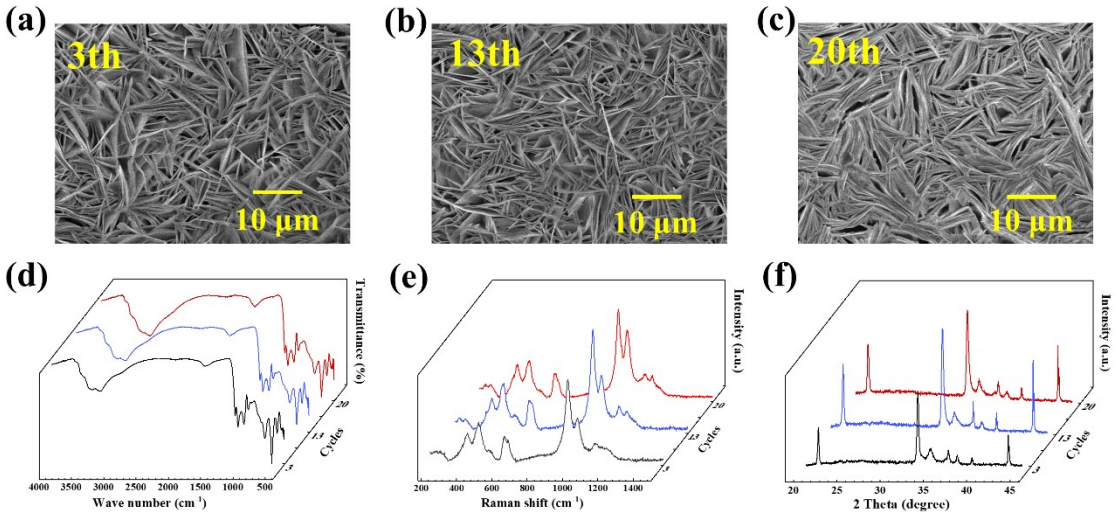

Fig. S7. The stability characterization of Zn-LDH electrode. (a-f) The SEM (a-c), characteristic peak changes in FTIR spectra (d), Raman spectra (e), and XRD pattern (f) after 3, 13, and 20 cycles. Fig. S7a-c† shows that a new phase on the zinc surface remains a two-dimensional sheet structure after 3, 13, and 20 cycles. Fig. S7d-f† shows that the characteristic peaks position and intensity of Zn-LDH material in FT-IR, Raman, and XRD change hardly with the increase of charge and discharge cycles. Obviously, Zn-LDH shows pretty stability in the GCD.

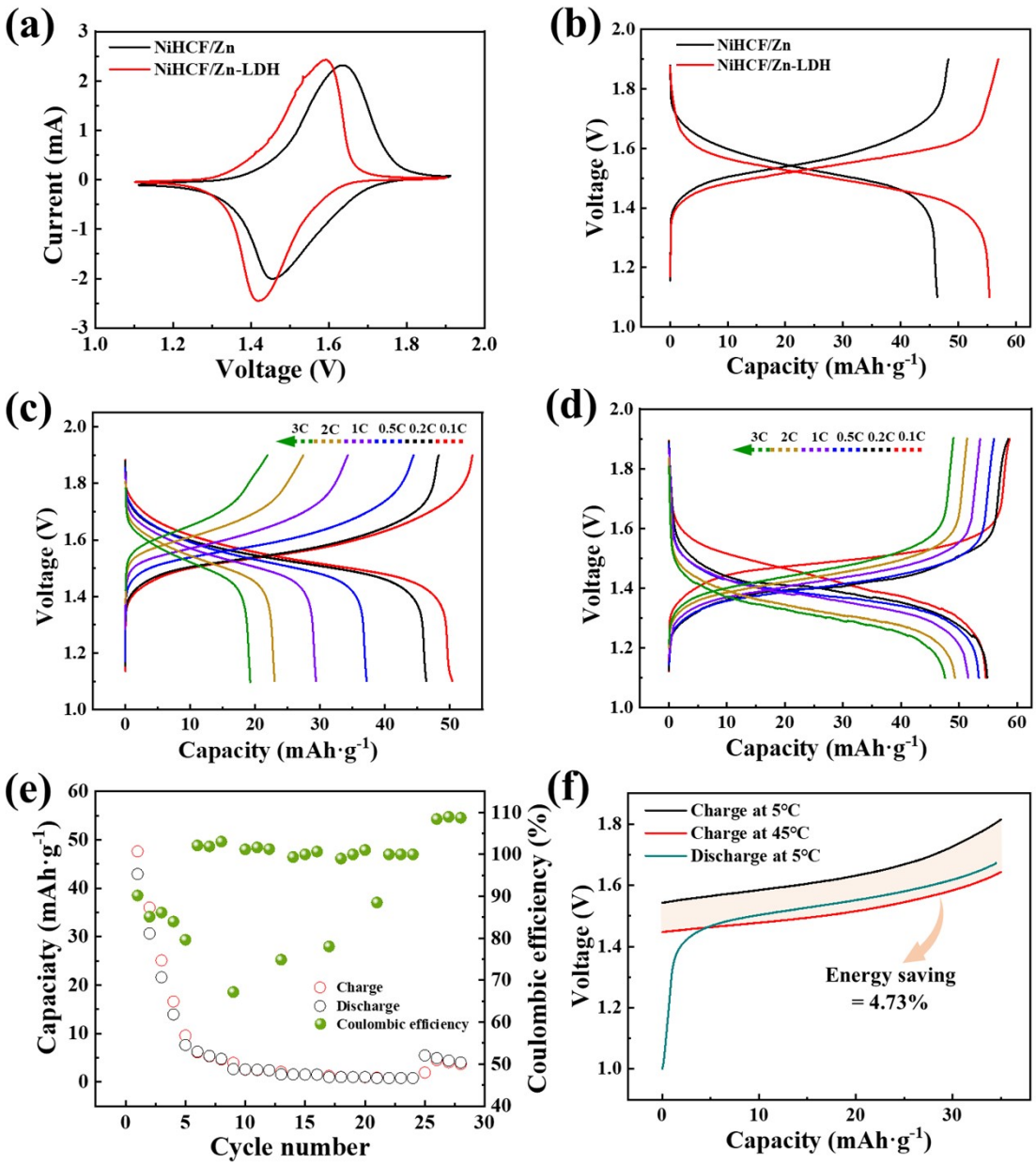

Fig. S8. Electrical performance in the NiHCF/Zn and NiHCF/Zn-LDH batteries. (a) Cyclic voltammetry curves at 0.5mV·s^{-1}. (b) Galvanostatic charge and discharge curves (0.2C). (c, d) The GCD curves with various current densities in NiHCF/Zn (c) and NiHCF/Zn-LDH (d) batteries. (e, f) Rate performance and capacity reversible performance (e) and energy saving in the heat charging at 0.2C (f) of the NiHCF/Zn battery. Fig. S8a,b† shows that the two systems have almost the same oxidation and reduction potential and capacity at room temperature. However, NiHCF/Zn-LDH battery has lower battery polarization than NiHCF/Zn due to the thermodynamic advantage brought by the introduction of reversible reaction in the Zn-LDH electrode.

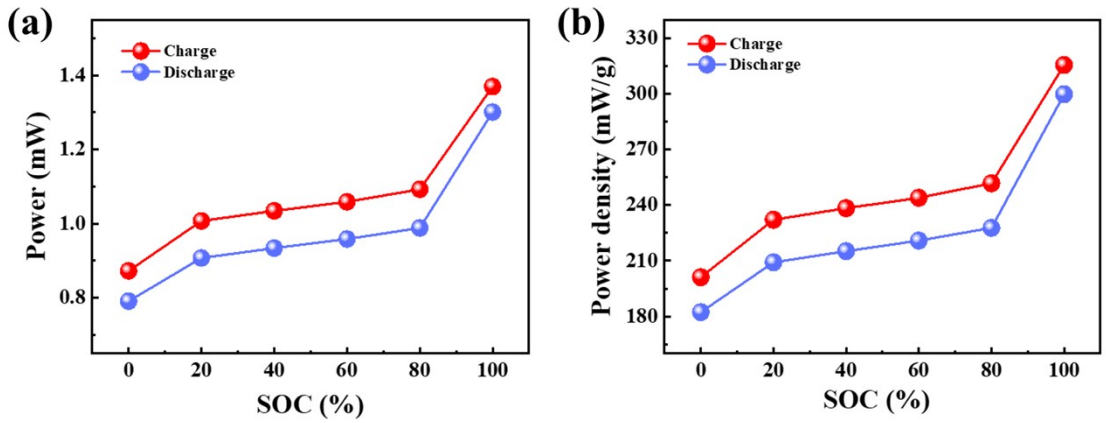

Fig. S9. (a) Power and (b) Power density changes with the state of charge (SOC) of the NiHCF/Zn-LDH battery during the charging and discharging process. The constant current is 0.72 mA (current density of 168 mA/g). It shows that the power and power density all increase with the battery's SOC. At 100% SOC, the maximum power and power density are 1.37 mW and 315.59 mW/g, respectively, when the charging voltage is 1.85V.

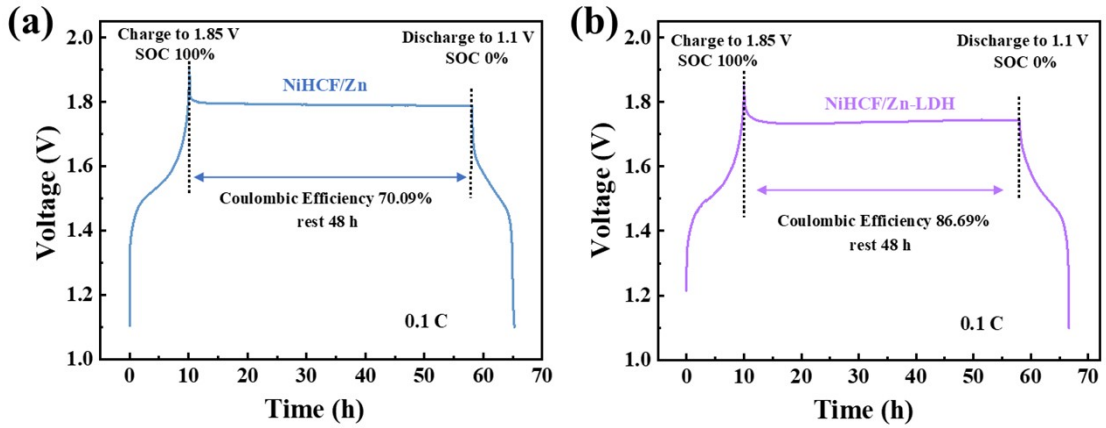

Fig. S10. The self-discharge test of (a) NiHCF/Zn and (b) NiHCF/Zn-LDH batteries. It indicates that the LDH material isolates oxygen and water to avoid side reactions, leading to the improved self-discharge performance of the NiHCF/Zn-LDH battery.

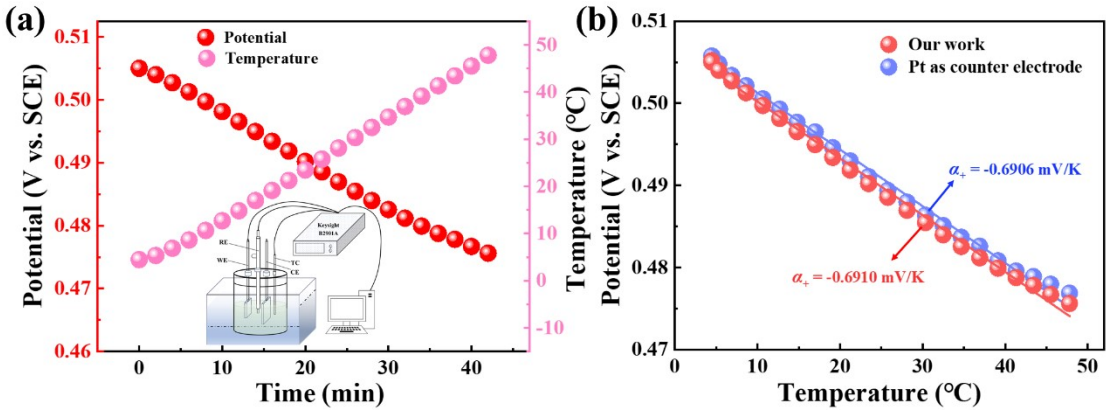

Fig. S11. The measurement of the temperature coefficient. (a) The potential of the NiHCF and temperature as a function of time, respectively (inset shows a schematic diagram of the testing device). (b) The *α* of the NiHCF in our work and Pt as the counter electrode in the three-electrode NiHCF/Zn-LDH system. The potential of the WE relative to RE was measured as a function of temperature when Pt was used as the counter electrode and current passed through it (Fig. S11b†). It shows that the temperature coefficient error of the cathode measured by the two testing methods is less than 0.06%.

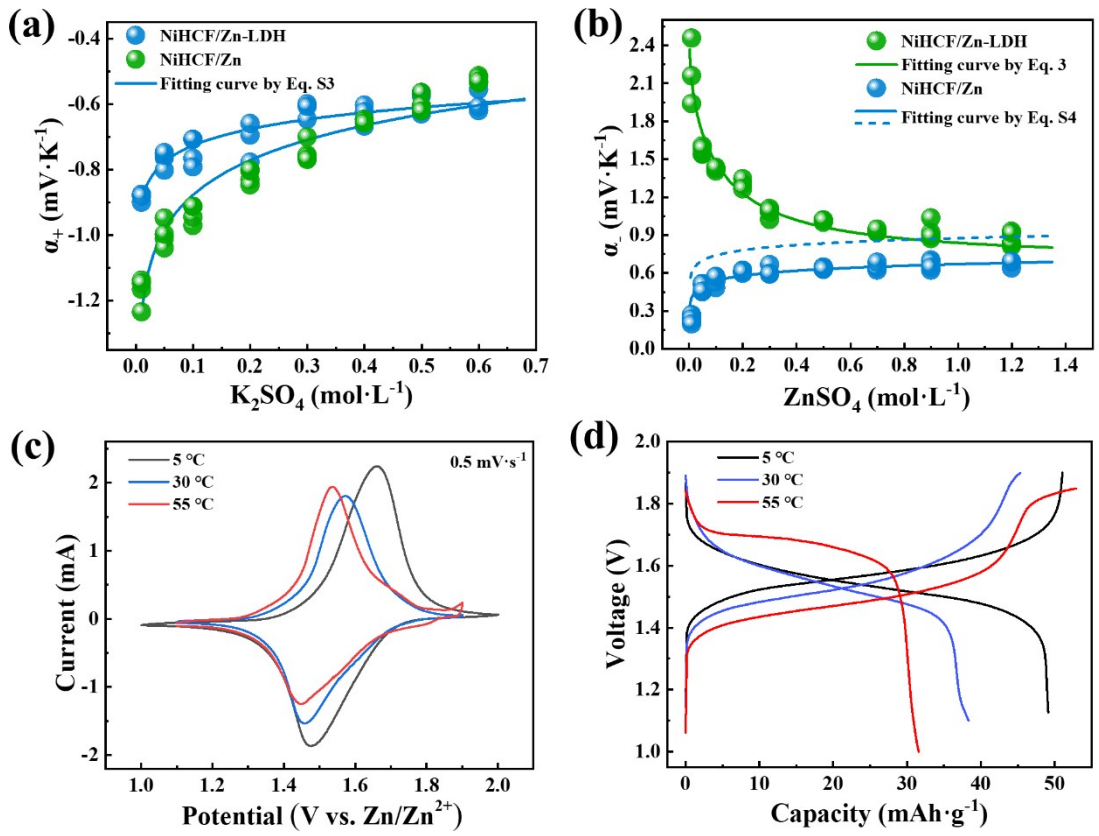

Fig. S12. Various temperature performance in the NiHCF/Zn and NiHCF/Zn-LDH batteries. (a) The dependence of a_+ on the K_2SO_4 concentration. (b) The dependence of a_- on the $ZnSO_4$ concentration. (c, d) Cyclic voltammetry curves (c) and galvanostatic charge and discharge curves (d) at 10℃, 30℃, and 55℃, respectively (0.2C) in the NiHCF/Zn battery.

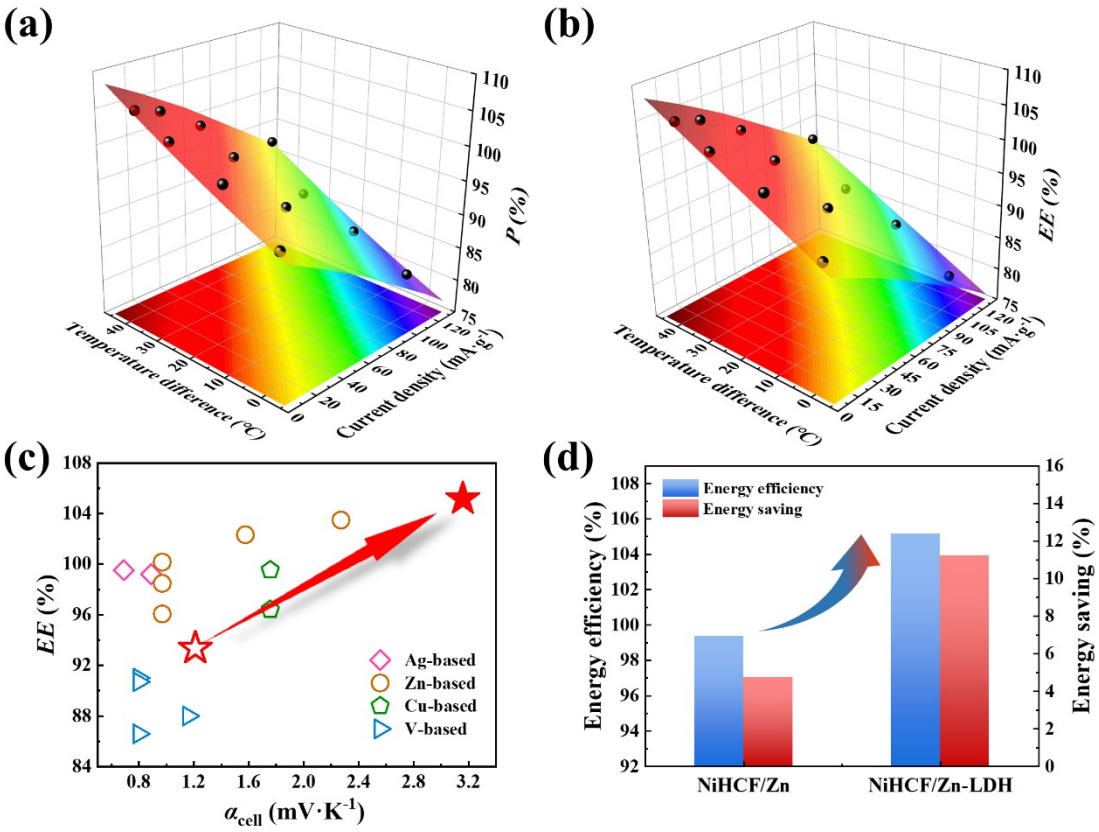

Fig. S13. (a, b) *P* values (a) and *EE* values (b) under different current densities and temperature differences; the color surface is fitted by the experimental data (black ball). (c) Energy efficiency *vs* α_{cell}. The hollow star and the solid star represent the data in NiHCF/Zn and NiHCF/Zn-LDH batteries, respectively. The others are taken from references 23-37. (d) Energy efficiency and energy saving in the heat charging at 0.2C of the NiHCF/Zn and NiHCF/Zn-LDH battery. The color surface fitted by the experimental data further illustrates that the battery has larger *P* and *EE* values at higher heat charge temperatures and lower current densities.

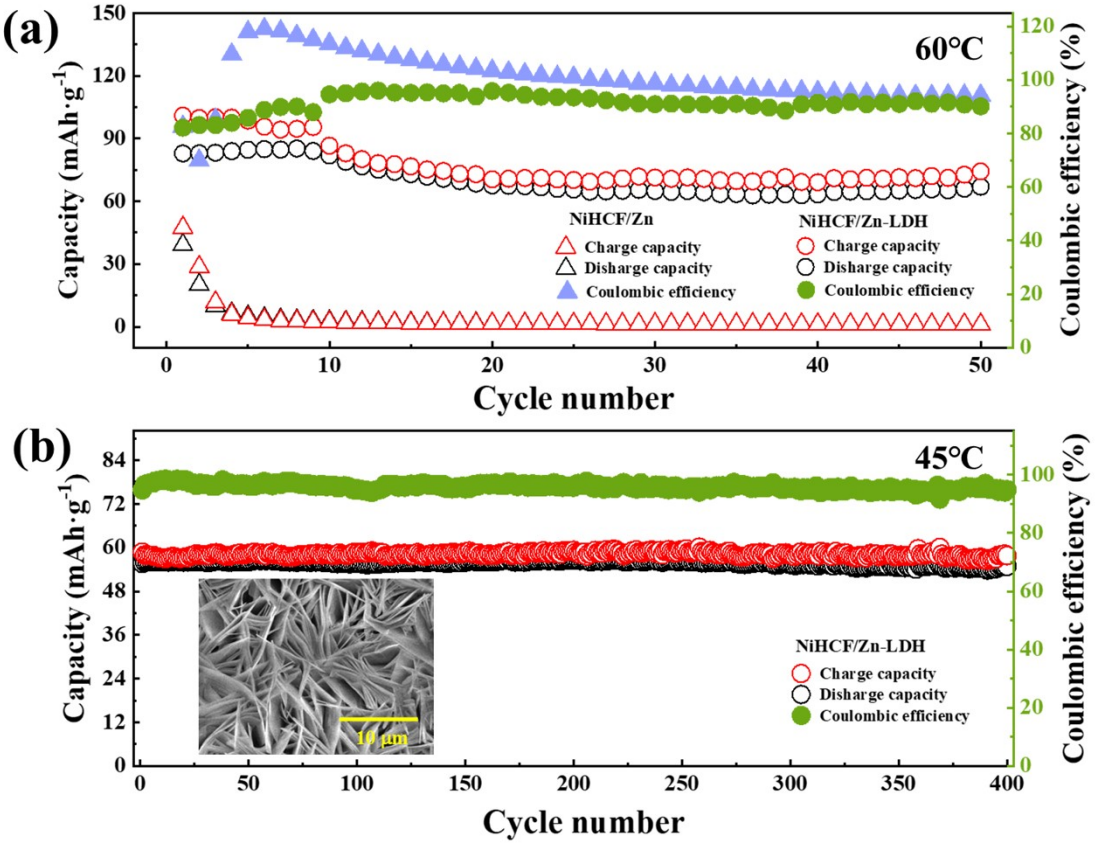

Fig. S14. High-temperature stability of galvanostatic charge-discharge (GCD) at 2C (a) NiHCF/Zn and NiHCF/Zn-LDH batteries at 60 ℃, (b) NiHCF/Zn-LDH battery at 45 ℃ (inset shows the SEM characterization of the Zn/Co-LDH electrode after 400 cycles).

The capacity of the NiHCF/Zn battery decreases to 2.63% after 50 cycles of GCD at 60 ℃, showing poor high-temperature stability. Similarly, the capacity of the NiHCF/Zn-LDH battery decreased by 19.21% after 50 cycles, showing poor stability at 60 ℃. Fig. S14b† shows that the Zn/Co-LDH electrode maintains a layered structure after GCD for 400 cycles at 45℃, indicating the excellent stability of the Zn/Co-LDH electrode. Moreover, the NiHCF/Zn-LDH battery has a low risk of thermal runaway due to the operation temperature lower than 50 ℃ and stable electrodes and electrolyte of aqueous Zn-ion batteries. Due to the high negative α, the higher the temperature, the lower the voltage of the battery, resulting in smaller output power and suppressing the positive feedback of heat and electricity. Therefore, the NiHCF/Zn-LDH battery has excellent thermal stability and minimal risk of thermal runaway during thermal charging.

Supplementary Table

Table S1. Performance of the NiHCF/Zn-LDH battery at different current densities and temperature differences.

I **(mA·g^{-1})**	**Heat charge temperature (℃)**	**Q_{charge}** **(mAh·g^{-1})**	**Coulombic efficiency (%)**	***P*** **(%)**	***EE*** **(%)**
11.2	45	39.10	99.99	105.16	105.16
28	45	39.04	99.99	103.99	103.98
56	45	40.04	99.98	100.16	100.14
112	45	39.99	99.98	93.97	93.96
11.2	35	40.01	99.99	102.62	102.62
11.2	20	40.02	99.98	99.77	99.75
11.2	5	39.91	99.22	94.09	93.35
56	35	40.03	99.99	97.34	97.33
56	20	40.02	99.99	93.07	93.06
112	35	40.04	99.99	87.60	87.59
112	20	40.04	99.99	84.77	84.76
112	5	41.13	97.84	81.47	79.71

References

1 R. Vedalakshmi, V. Saraswathy, H.-W. Song and N. Palaniswamy, *Corros. Sci.*, 2009, **51**, 1299-1307.

2 J.-M. Huo, Y. Wang, J.-N. Xue, W.-Y. Yuan, Q.-G. Zhai, M.-C. Hu, S.-N. Li and Y. Chen, *Small*, 2024, **20**, 2305877.

3 Y. Liao, R. He, W. Pan, Y. Li, Y. Wang, J. Li and Y. Li, *Chem. Eng. J.*, 2023, **464**, 142669.

4 W. Li, G. Wang, C.